ACS APPLIED MATERIALS & INTERFACES

RESEARCH ARTICLE

www.acsami.org

Fabrication, Growth Mechanism, and Characterization of α-Fe_2O_3 Nanorods

Gajendra K. Pradhan and K. M. Parida*

Colloids and Materials Chemistry Department, Institute of Minerals & Materials Technology (CSIR), Bhubaneswar-751013, Orissa, India

ABSTRACT: This work reports the facile synthesis of α-Fe_2O_3 nanorods and nanohexagons and its application as sunlight-driven photocatalysis. The obtained products were characterized by X-ray diffraction (XRD), transmission electron microscopy (TEM), selected area electron diffraction (SAED), scanning electron microscopy (SEM), diffused reflectance spectroscopy (DRUV-vis), Fourier transform infrared spectroscopy (FTIR), and X-ray photoelectron spectroscopy (XPS). The phase and crystallinity were confirmed from the XRD study. Electron microscopy study clearly indicates the formation of different morphologies of nanocrystals. These hematite nanostructures were used as a model system for studying the shape-dependent photocatalytic degradation of phenol, methylene blue, and congo red. Amongst all the nanostructured semiconductors, Pt-doped hematite nanorod showed 55% efficiency towards the decolonization of methylene blue and 63% toward congo red under sun light illumination. The difference in photocatalytic activity is discussed in terms of their crystallize size and morphological ordering.

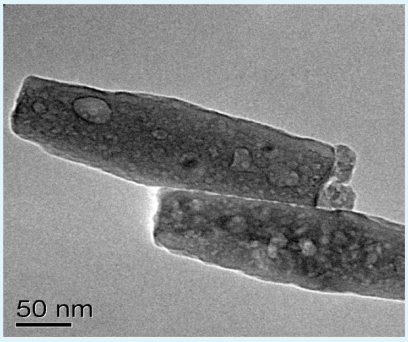

KEYWORDS: hematite, nanorods, shape, decolorization

INTRODUCTION

Fabrication of architectural one-dimensional (1D) iron oxide nanostructures are still a challenging and important research subjects in nanoscience and nanotechnology because of their unique size- and shape-dependent properties. Iron oxide with different morphology such as nanospheres, nanorods, nanowires, nanotubes, nanonecklaces, nanorices, airplanes, tetrapods, peanuts, nanoflower, and nanospindles have been reported previously in the literature.[1−14] Wu et al. fabricated the α-Fe_2O_3 nanorod (700 nm) using Fe-$(C_5H_7O_2)_3$ and deposited on silicon substrate by chemical vapour deposition method.[3] Almeida and co-workers reported the hydrothermal synthesis of lenticular nanorod and pseudocubes of α-Fe_2O_3 using $FeCl_3$ and $NH_4H_2PO_4$.[4] Various surface directing agents such as NaH_2PO_4 and $NH_4H_2PO_4$ have been used previously for the synthesis of different shapes of α-Fe_2O_3.[7,14]

Geometrical configuration and elemental composition of this 1D system is very useful for different applications. In particular, iron oxide has been widely investigated because of their applications as catalysis, sensors, pigments, magnetic resonance imaging (MRI), drug-delivery, photocatalysis, and photoelectrochemical cell.[1,15−22] The high absorptive power of hematite in the visible range could be utilized for various photocatalytic applications. The limitations over photocatalytic application comprise the low band gap energy (2.2 eV), poor conductivity and high electron-hole (e^--h^+) recombination. To address these issues, researchers have taken into consideration incorporation of heteroatom (e.g., Si, Bi, Pt, and Ta), quantum confinement, and architectural control.[23−27] In 1D nanostructure, the electrons are channelized and have very good electron transporting ability which minimizes the e^--h^+ recombination.[21,28] This makes the material photoactive. However a few works have been reported on dye degradation over different-shaped iron oxide.[13,14]

Herein, we report the hydrothermal synthesis of α-Fe_2O_3 nanorod, nanosphere and nanohexagon using $(NH_4)_2HPO_4$ as the surface directing agent. The effect of reaction time and the effect of different surfactants on the synthesis of nanorods have been investigated. In addition to this, solar-light-driven photocatalytic activity towards dye and phenol degradation has been studied over the synthesized material. The novelty of synthesis and highly photocatalytic activity of uniform diameter nanorods are explained with the help of various spectroscopic techniques. To the best of our knowledge, this is the first ever report on facile fabrication of hematite nanorod for photodegradation of phenol, methylene blue, and congo red.

EXPERIMENTAL SECTION

Materials. All the chemicals and reagents are of analytical grade and used without further purification. Iron(III) chloride hexahydrate, diammonium hydrogen phosphate, sodium dodecyl sulphate (SDS), deionized water, and polyethylene glycol (PEG) were used for the sample preparation. Commercial Fe_2O_3 was used for catalytic reaction.

Received: October 1, 2010
Accepted: December 7, 2010
Published: January 7, 2011

Methods. In a typical experiment, stoichiometric amounts of $(NH_4)_2HPO_4$ were added to aqueous solution of $FeCl_3 \cdot 6H_2O$, under vigorous stirring until a yellow homogeneous solution was obtained. The solution was then sealed into a Teflon-lined autoclave, followed by hydrothermal treatment at 220 °C for 36 h (S1). Also the experiment was performed for 12 and 24 h in the same reaction condition and named as S5 and S6, respectively. Samples were also prepared in the presence of SDS and PEG and noted as S2 and S3, respectively. Platinum doping was done without use of any surfactant by taking $PtCl_6$ and maintaining the ratio of Fe/Pt as 100:1 and is denoted as S4. After the treatment, the products were collected by centrifugation, filtered, washed several times with deionized water, and dried at 110 °C for overnight. The dried samples were calcined at 400 °C for 3 h.

Characterization. Phase identification was carried out using a PANalytical X-ray diffractometer with Mo Kα radiation (λ = 0.70932 A°) in the 2θ range from 10 to 40°. Low-angle XRD was done using a Rigaku X-ray diffractometer with Cu Kα radiation (λ = 1.54 Å) in the 2θ range from 0 to 10° to check the mesoporous nature of the material. FTIR spectra were recorded in a Varian FTIR spectrophotometer (FTS-800) in the range of 400−4000 cm^{-1}, taking KBr as the reference. The optical absorbance was observed by UV−visible diffuse reflectance spectra (Varian, Cary 100). Surface morphology of the samples were studied through a transmission electron microscope (FEI, TECNAI G^2 20, TWIN, Philips) operating at 200 kV. The samples for electron microscopy were prepared by dispersing in ethanol and coating a very dilute suspension in carbon coated Cu grids. TEM images were recorded by using Gutan CCD camera. The surface morphologies were also examined through a scanning electron microscope (SEM, Hitachi S-3400N) by collecting secondary electron images at 15 kV. The samples were coated with gold to make the surface conducting before putting into the SEM chamber. The electronic states of Fe were examined by X-ray photoelectron spectroscopy (XPS, Kratos Axis 165 with a dual anode (Mg and Al) apparatus) using the MgKα source. All the binding energy values were calibrated by using the contaminant carbon (C1s = 284.9 eV) as a reference. Charge neutralization of 2 eV was used to balance the charge of the sample. Binding energy values of the samples were reproducible within ±0.1 eV. The surface area and pore diameter were measured by N_2 adsorption−desorption technique at −196 °C in automated surface area and porosity analyser (ASAP 2020, Micromeritics, USA). Prior to the analysis, samples were degassed under a vacuum (1×10^{-5} Torr) at 300 °C for 4 h.

Photocatalytic Reaction. The photoefficiencies of all synthesized catalysts were tested toward degradation of phenol, congo red (CR), and methelene blue (MB) under solar radiation. In a typical experiment, 30 mg of catalyst with 20 mL of 10 ppm phenol solution was taken in a 100 mL closed Pyrex flask. The solutions were exposed to sunlight with constant stirring for 4 h. In a similar fashion, 20 mg of catalysts were suspended in 20 mL of 100 ppm CR and MB solution for photoexperiments under identical conditions. After irradiation, the suspension was centrifuged and the concentration of the supernatants was analyzed quantitatively at 504 nm (λ_{max} for phenol), 664 nm (λ_{max} for methylene blue), and 500 nm (λ_{max} for congo red) using a Cary-100 (Varian, Australia) spectrophotometer. All the catalytic results were reproducible with ±4% variation. The intensity of solar light was measured using a Digital Illuminance Meter (model TES-1332A, Taiwan). During the measurement, the sensor was set in such a position where the intensity was maximum. The average light intensity was around 100 000 lux, which was nearly constant (10AM−2PM) during the experiments.

RESULTS AND DISCUSSION

Mechanism of Formation of Hematite. Fabrication of α-Fe_2O_3 nanoparticle is achieved by using its chloride salt as precursor and $(NH_4)_2HPO4$ as the precipitating agent (Scheme 1). Because of the amphoteric character of water, the electropositive cation (Fe^{3+}) induces the H_2O ligand and forms a hexa aquo complex. The complex leads to breakage via deprotonation and gives rise to $FeOH(H_2O)_5^{2+}$, $Fe(OH)_2(H_2O)_4^{+}$, and finally an oxide hydroxide product of iron (FeOOH) is formed.[29] On heat treatment, the oxide hydroxide species yields α-Fe_2O_3.

Scheme 1 . Formation Mechanism of α-Fe_2O_3

$$FeCl_3 + 6\,H_2O \rightarrow Fe(H_2O)_6^{3+} + 3\,Cl^-$$

$$Fe(H_2O)_6^{3+} \rightarrow FeOOH + 3\,H^+ + 4\,H_2O$$

$$2\,FeOOH \rightarrow \alpha\text{-}Fe_2O_3 + 2\,H_2O$$

Scheme 2 . Effect of Surfactant on the Formation of Different Shape of α-Fe_2O_3

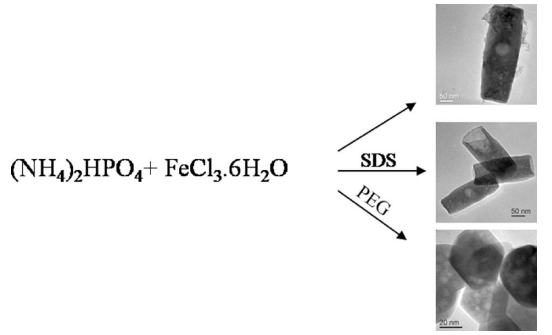

Mechanism of Formation of Different-Shaped Hematite Nanostructure. Hydrothermal method is considered to be the best technique for the control of different nanostructures. Various morphological nanopaticles have been fabricated with this method as reported by many researchers.[4,30,31] Although the formation mechanism of different shapes of nanoparticles have not been established to date, herein we have made some attempts to propose the mechanism that is as follows: The addition of $(NH_4)_2HPO_4$ to the aqueous solution of hydrated ferric chloride gives a homogeneous yellowish solution. The decomposition of $(NH_4)_2HPO_4$ leads to NH_4^+, PO_4^{3-} ion, which plays a pivotal role for the formation of different shape of hematite. The released ammonia is acting here as a precipitating agent. It controls the nucleation as well as growth of small iron oxide particles. However, growth of nanocrystal was preferentially controlled by the PO_4^{3-} anion.[18] The effect of different nanostructure in absence and presence of surfactant is presented in Scheme 2 .

XRD. X-ray diffraction technique can yield a great deal of structural information, phase identification, about materials under investigation. Figure 1 shows the XRD patterns of the 400 °C calcined samples (S1, S2, S3, and S4). It shows that the particles are well crystallized in a single phase. All of the diffraction peaks can be indexed to rhombohedral α-Fe_2O_3 (JCPDS 13-534). No impurity peaks for FeOOH, Fe_3O_4, γ-Fe_2O_3 is present in the pattern. The multiple peaks evidence the polycrystalline nature of all the synthesized material. The XRD peak in the low-angle region (Figure 2) at $2\theta \approx 0.43$ and 0.86° claims the material is mesoporous. The crystallize size of all the

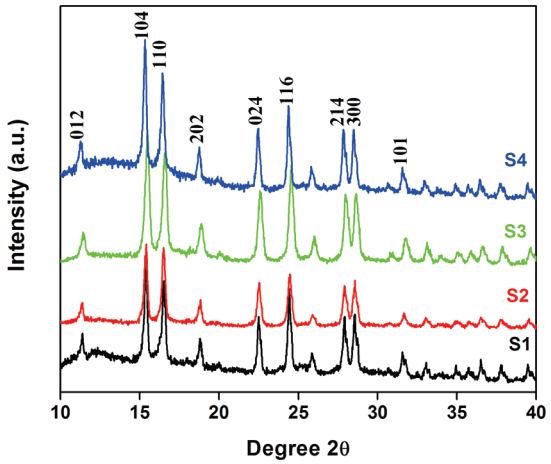

Figure 1. XRD patterns corresponding to samples S1, S2, S3, and S4 calcined at 400 °C (With miller indices corresponding to α-Fe_2O_3).

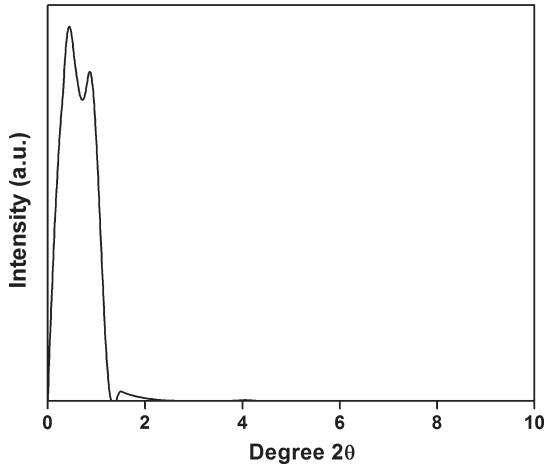

Figure 2. Low-angle X-ray diffraction (LAXRD) of sample S1 calcined at 400 °C.

samples were measured using Scherrer formula

$$D = K\lambda / \beta \cos\theta$$

where λ is the wavelength of the MoKα used, β is the full width at half maximum of the diffraction angle considered, K is a shape factor (0.94), and θ is the angle of diffraction. The crystallite sizes of S1, S2, S3, and S4 are 18.314, 17.027, 17.481, and 17.025 nm, respectively. To clarify the crystal structure of particles, the unit-cell dimension of the synthesized samples was measured (Table 1). Both the *a*-edge and *c*-edge length of the synthesized materials were lower than the reported value.[29]

SEM. The scanning electron micrographs of the samples are depicted in Figure 3. To investigate the evolution process of the α-Fe_2O_3 nanorods, time-dependent experiments were carried out. Reactions were carried out at 12 h (S5), 24 h (S6), and 36 h (S1) in the presence of only $(NH_4)_2HPO_4$. There is incomplete growth of such nanorod shaped materials observed at 12 and 24 h. Reaction time is one of the key factors for the growth of a crystal of particular shape. Here reaction time might not be enough to grow to the final morphology of the product. When the reaction time was prolonged to 36 h (sample S1), well-dispersed nanorods were observed and have rod-shaped morphology. We kept this reaction time as optimum for all the other reactions. To check the effect of surfactants on surface structure, we added surfactants like SDS and PEG, keeping all the reaction conditions same. The addition of SDS (sample S2) doesn't affect the surface structure of the nanorod. However, when the system was added with PEG (S3), hexagonal-shaped nanoparticles were obtained. So PEG plays a major role for the growth and formation of nanosphere and nanohexagon. Pt-doped sample (S4) also retains the surface topography after the addition of $PtCl_6$.

Table 1. Average Crystallite Size, Aspect Ratio, Unit-Cell Parameters, and Photo Degradation Activity of All the Synthesized Sample

					% of degradation		
sample name	crystallite size (nm)	aspect ratio	*a* (nm)	*c* (nm)	phenol	MB	CR
Fe_2O_3					2 ± 0.5	20 ± 1	27 ± 3
S1	18.314	2.74	4.887	13.485	5 ± 2	45 ± 1	56 ± 3
S2	17.027	3.38	4.825	13.371	7 ± 1	48 ± 3	59 ± 2.5
S3	17.481		4.750	13.241	4 ± 3	39 ± 4	46 ± 4
S4	17.025	3.32	4.801	13.339	12 ± 2	55 ± 4	63 ± 3

TEM. To extensively investigate the morphology of the nanostructures, we carried out bright-field (BF) TEM experiments. The TEM images of the nanostructures are shown in Figure 4. In addition to the nanostructures, small irregular fragments are also appeared in the pictures, which might have originated during the processing and/or sonication of nanorods for TEM scanning. Consistent with SEM observations, the nanostructures have the shape of rods having average length and average diameters of 294 and 107 nm (Figure 4(S1)). Therefore, the aspect ratio is around 2.74. The aspect ratio of the nanostructures is not too high. This may be due to the agglomeration of particulates in both longitudinal and lateral direction during the synthesis. However, the longitudinal growth is faster than the lateral one. In addition, there are no side-branches and cross-linking between the nanorods, which is a major advantage for the controlled process and use of single nanorod in some specific applications. The formation of nanorod might be due to the slow precipitation of iron oxide by NH_3. Here phosphate (PO_4^{3-}) is responsible for the formation of nanorod and allows the growth mainly along the [104] and [110] plane as seen from XRD. The aspect ratio of nanorods (3.38) (Figure 4 (S2)) are little higher than those shown in Figure 4 (S1), which is due to the reduced in lengths and diameters (284 and 84 nm, respectively). The reduction in diameter (Fig 4 (S2)) depicts that the nanoparticles are preferably agglomerated along longitudinal direction. The addition of SDS does not affect the surface morphology of nanorod. The dominance of phosphate group over sulphate is expected on growth along the above mentioned two planes as described for S1. In sample S3, the nanostructures are hexagonal shape, which may be due to the agglomeration of particles are almost same in each direction. The diameter of the spherical structures is around 53 nm. The addition of PEG having −OH groups strongly competes with PO_4^{3-} group, acts as a destructive reagent, and does not help in growing the nanorod-shaped structure. This may lead to a change in the nanorod-shaped topography to

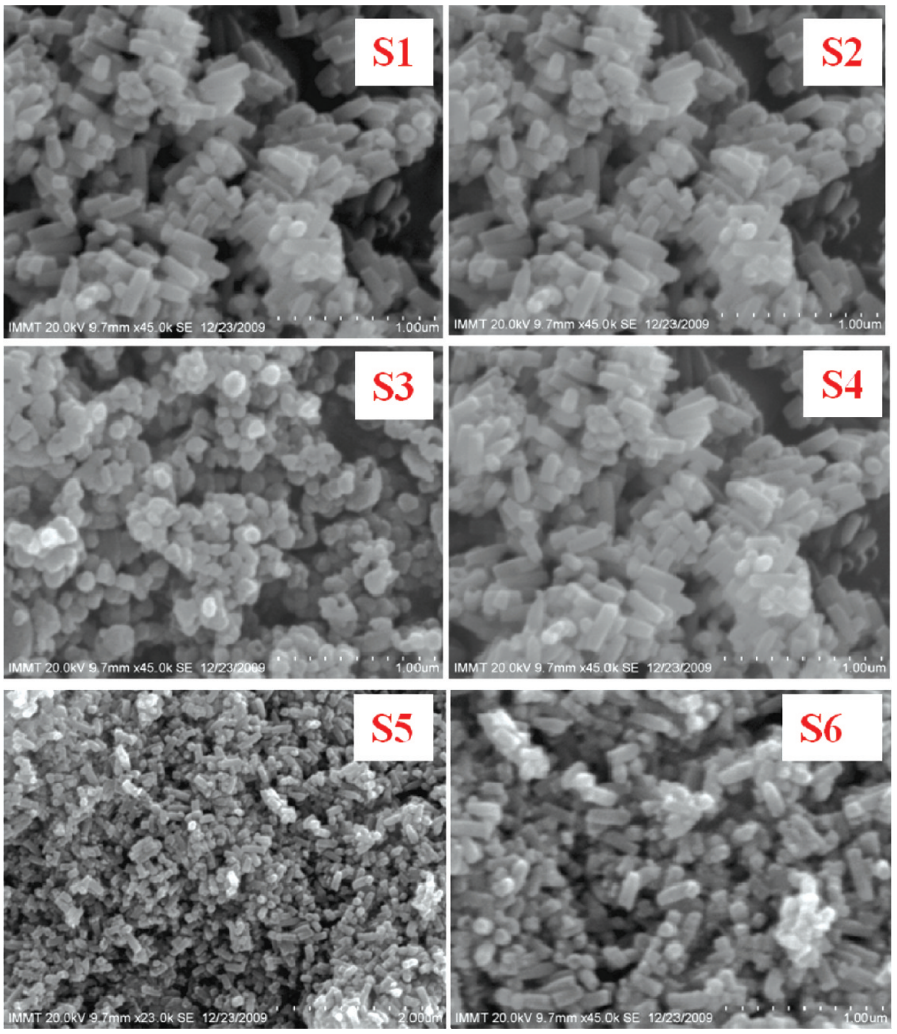

Figure 3. Typical SEM images of samples S1, S2, S3, S4, S5, and S6 calcined at 400 °C.

hexagon shape. The hydroxyl group dominates over the phosphate group and allows the formation of hexagon shaped particle after the nucleation. In sample S3, there are two kinds of particle, hexagon shape and something other than hexagon shape. We are expecting the first type to be completely grown, whereas the growth is not completed in the later type. Nanorods with smaller diameter, as observed in case of the sample S4. The average length, diameter, and aspect ratio are 286 nm, 86 nm, and 3.32 respectively. In addition, the surface of nanostructues seems to be little rough with the evolution of bigger particles. This may be due to the formation of nonuniform tiny particulates at very initial stages and afterwards they agglomerate to give bigger nanostructures with various shapes and sizes. From the above observations, it is clear that the use of surfactant has an ability to change the morphology of nanostructures. The SAED pattern inserted in the TEM figure of S1, S2, S3, and S4 explains the polycrystalline nature of all the samples.

UV−Vis DRS. UV−vis DRS spectra of all the samples are shown in Figure 5. There are three prominent absorption bands observed at 274, 364, and 537 nm in the UV−vis DRS spectra. The first peak may be assigned to metal to ligand charge transfer spectra. The next two peaks correspond to $^6A_1 \rightarrow {}^4E$ and $2(^6A_1) \rightarrow 2(^4T_1)$ ligand field transition of Fe^{3+}, respectively. Also the finger print region of the band edge of hematite is 521−565 nm, whereas in all the synthesized samples from S1 to S4 the band edge observed from 530−574 nm.[29] This is in good agreement with the XRD results, i.e., all the samples are α-Fe_2O_3.

XPS. To investigate the chemical environment and electronic structure of the elements present in the sample, we carried out X-ray photoelectron study. XPS spectra of sample S1 are depicted in panels a and b in Figure 6. To identify all the states of oxygen and iron, we deconvoluted both the O 1s and Fe 2p. The deconvolution peaks (Figure 6a) of O 1s spectrum were observed at 529.8, 531.5, 533, and 534.8 eV, respectively. The low binding energy (BE) component observed at 529.8 eV is attributed to the O^{2-} forming oxide with iron whereas the later three components were assigned to OH^-, C−O and O−C═O, and H_2O, respectively.[32,33] Similarly, the core level spectra of Fe 2p were curve fitted and are shown in Figure 6b. There are five multiplet peaks for Fe 2p observed in the spectra. Peaks corresponding to 708.8 (A) and 720.9 eV (D) are attributed to +2 oxidation states, whereas 710.8 (B) and 723.6 eV (E) are ascribed to +3 states of iron. The peak with BE of ∼715.6 eV (C) is identified as the surface peak of α-Fe_2O_3.[34]

FTIR. FTIR graphs of S1, S2, S3, and S4 are presented in fig.7. Characteristic absorption bands at 2361 cm^{-1} is assigned to C═O stretching for atmospheric CO_2.[35] Another distinct peak at 1390 cm^{-1} is ascribed to bending frequency of surface hydroxyl

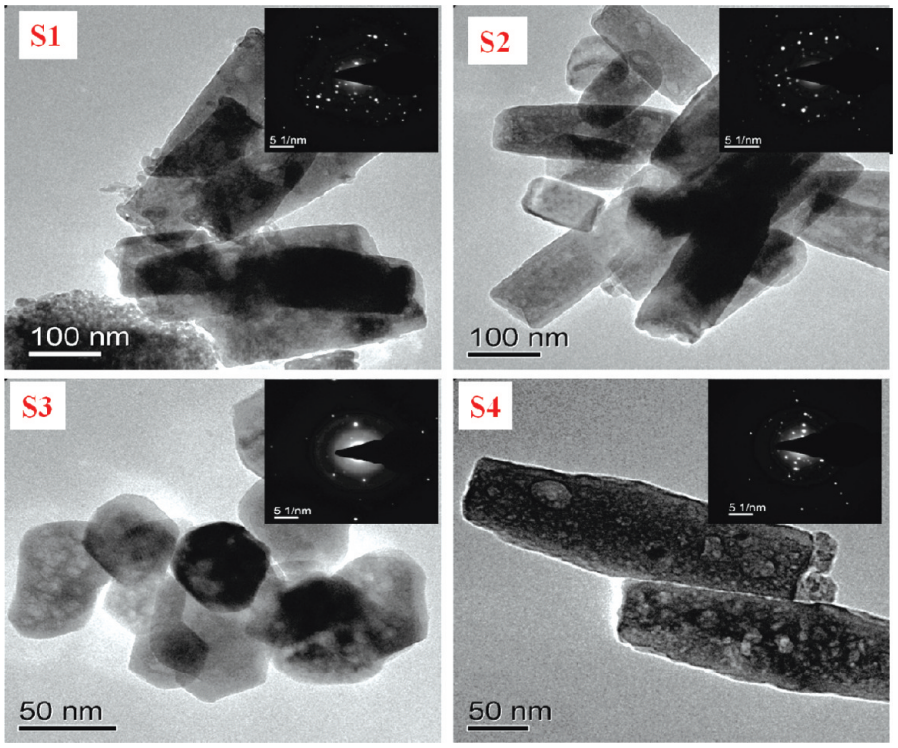

Figure 4. (S1) Representative TEM image of α-Fe_2O_3 iron oxide nanorod obtained from $FeCl_3 \cdot 6H_2O$ and $NH_4H_2PO_4$, (S2, S3) Influence of SDS and PEG on the shape of nanocrystal, (S4) 1% Pt-doped iron oxide.

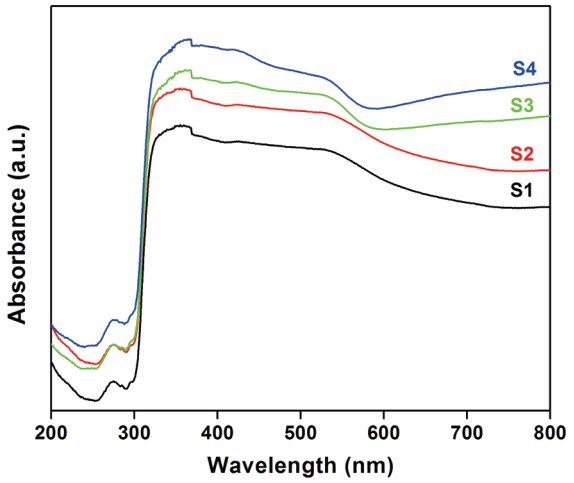

Figure 5. UV−vis spectrum of samples S1, S2, S3, and S4 calcined at 400 °C.

group.[36] Zhao et al. attributed 536.57 and 460.09 cm^{-1} absorption bands to α-Fe_2O_3.[37] Li and coworkers claimed the bands of 570 and 480 cm^{-1} are due to Fe−O vibrational mode of α-Fe_2O_3.[38] In all the samples from S1−S4, the Fe−O vibrabational mode absorption band is observed in the range 464−468 cm^{-1}, which assures the hematite phase. These results agreed with the XRD, XPS, and UV−vis DRS results. The appearance of a weak peak in the region 1024 cm^{-1} confirms the presence of some phosphate impurity in all the samples.[39]

N_2 Adsorption−Desorption Isotherm. To know the surface area and porous nature of the material, we carried out N_2 adsorption−desorption isotherm for sample S1. The adsorption−desorption isotherm and pore size distribution are shown in panels a and b in Figure 8, respectively. The BET surface area of the catalyst was found to be 4.7 m^2/g. From the BJH graph, the pore volume and average pore diameter were found to be 0.034 cm^3/g and 29 nm, respectively. Although the material is not completely mesoporous like MCM-41 or SBA-15, the pore diameter is in the range of mesoporous material. The mesoporous nature of the material is also supported by LAXRD results.

Photocatalytic Study. The percentage of degradation of phenol, methylene blue, and congo red were investigated as a function of different catalyst (Figure 9). The decolorization performance of all the catalysts is presented in Table 1. The dye with the catalyst was directly exposed to the sun light for 4 h. Also the substrates were tested in presence of sunlight without catalyst. But the decolourization was neglible in absence of the catalyst. The percentage of photocatalytic degradation in all our catalysts follows the order Fe_2O_3 < S3 < S1 < S2 < S4 after 4 h of reaction in solar light. Comparison was done to check the efficiency of our synthesized catalyst. Here, bulk Fe_2O_3 shows lower activity compared to other synthesized 1D nano rod as well as spherical hematite. Crystallize size is one of the important factor which has crucial role for the catalytic activity. Here the crystallite size has a trend of S3 < S1 < S2 < S4 and the trend of photocatalytic activity is also same. This explains the pivotal effect of crystallite size towards the photocatalytic activity of all the synthesized material.[40] As compared to the previously reported cases, nanorod-shaped catalyst shows high photocatalytic activity. This is because the electron transport in the 1D nanorod is channelized and lowers the electron-hole (e^--h^+) recombination.[41] Sample S3 shows the lowest degradation as the particles are nanohexagon on which the recombination chances is more as compared to 1D nanorod. Sample S1 showing less degradation as compared to sample S2, this can be explained by

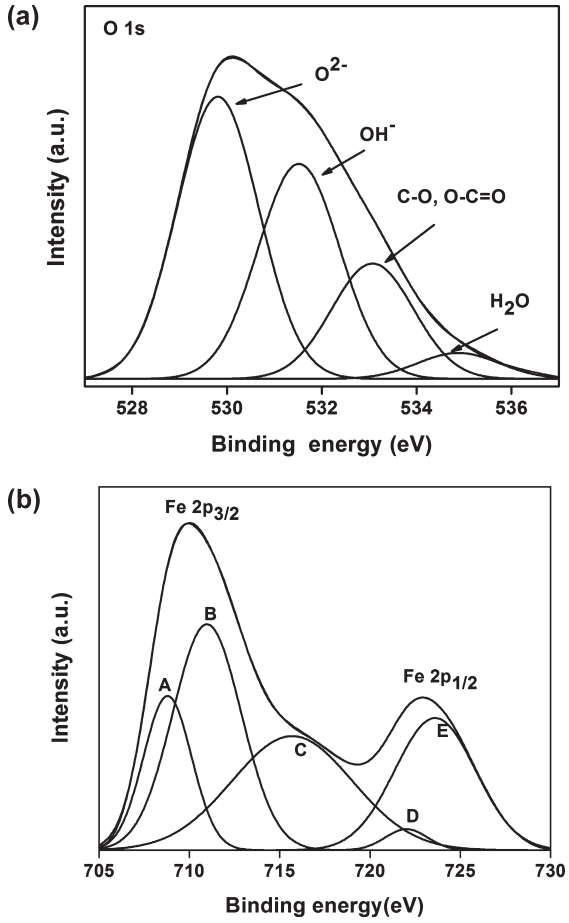

Figure 6. Survey XPS spectrum of α-Fe_2O_3 nanorod (S1): (a) high-energy-resolution O 1s core-level spectra and (b) high-energy-resolution Fe 2p core-level spectra.

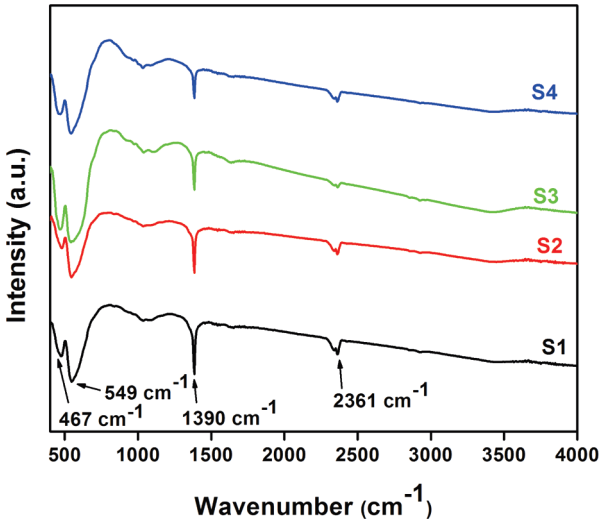

Figure 7. Fourier transform infrared spectra of S1, S2, S3, and S4 samples calcined at 400 °C.

comparing their aspect ratio. The aspect ratio of S2 (2.74) less than sample S1 (3.38). The lower aspect ratio might be responsible for the charge carrier recombination and hence decreases the efficiency of photocatalyst. The substitutions of Fe^{3+} by Pt^{4+}

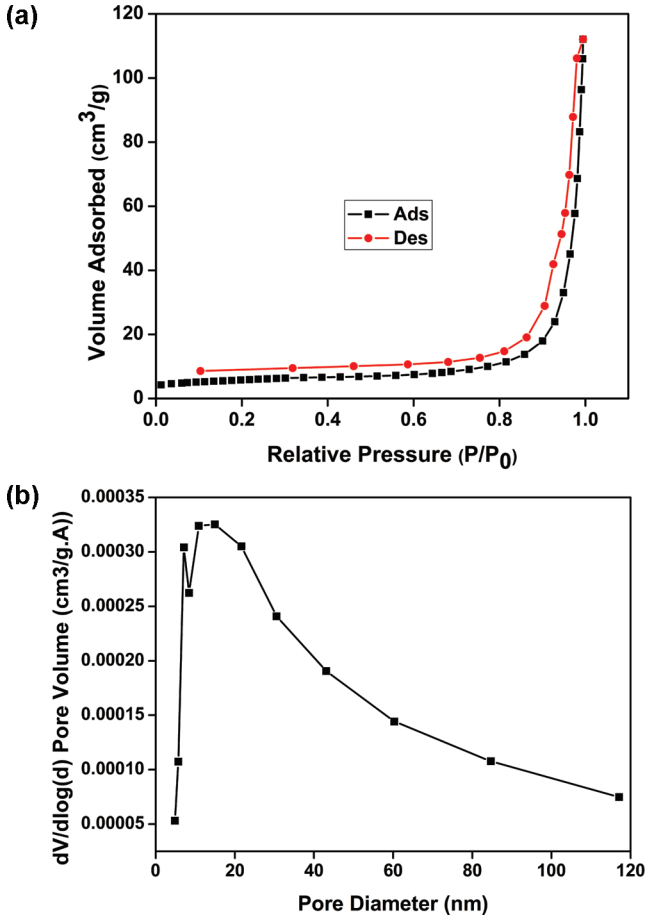

Figure 8. (a) BET isotherm of sample S1 calcined at 400 °C; (b) BJH isotherm of sample S1 calcined at 400 °C.

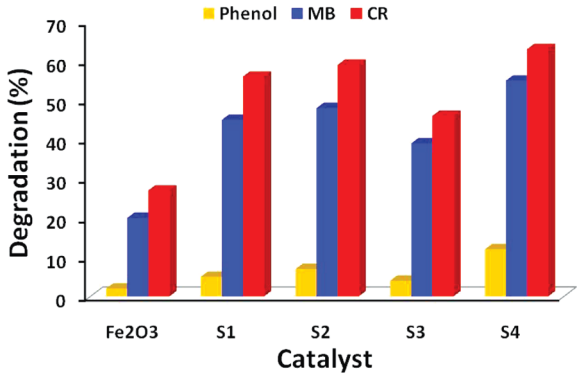

Figure 9. Photocatalytic degradation of phenol, MB, and CR over S1, S2, S3, and S4 catalysts in solar light.

increase the conductivity, enhance the charge transfer and hence decreases the e^--h^+ recombination. This is why it shows a higher percentage of photodegradation.

CONCLUSIONS

The main objective of this work is to synthesize one-dimensional α-Fe_2O_3 nanorods possessing uniform diameter so that electron transport can be channelized and electron-hole recombination can be delayed. We have successfully synthesized

α-Fe_2O_3 with different shapes via hydrothermal precipitation technique in presence and absence of surfactant using $(NH_4)_2$-HPO_4 as the structure-directing agent. The procedure employs low-cost raw material yielding a phase-pure, polycrystalline product. Degradation of phenol, methylene blue, and congo red were performed by the irradiation of solar light using catalyst of different morphology and in Pt-doped hematite nanorod. Our synthesized catalysts have better activity compared to bulk Fe_2O_3. Among various morphological samples, nanorod-shaped α-Fe_2O_3 shows highest photocatalytic activity for degradation of phenol and other dyes. Pt-doping on it further enhances the catalytic activity.

AUTHOR INFORMATION

Corresponding Author

*E-mail: paridakulamani@yahoo.com. Fax: 91674-2581637.

ACKNOWLEDGMENT

The authors are extremely thankful to Prof. B. K. Mishra, Director, IMMT, Bhubaneswar 751013, Orissa, India, for his constant encouragement and permission to publish the paper. We are highly grateful to Dr. K. S. Ramarao for doing LAXRD. The authors are also thankful to CSIR for providing financial assistance to Mr. G. K. Pradhan.

REFERENCES

(1) Liu, Q.; MinCui, Z.; Ma, Z.; Bian, S. W.; Song, W. G.; Wan, L. J. *Nanotechnology* **2007**, *18*, 385605.
(2) Deng, H.; Li, X.; Peng, Q.; Wang, X.; Chen, J.; Li, Y. *Angew. Chem., Int. Ed.* **2005**, *44*, 2782.
(3) Wu, J. J.; Lee, Y. L.; Chiang, H. H.; Wong, D. K. P. *J. Phys. Chem. B* **2006**, *110*, 18108.
(4) Almeida, T. P.; Fay, M.; Zhu, Y.; Brown, P. D. *J. Phys. Chem. C* **2009**, *113*, 186898.
(5) Han, Q.; Liu, Z.; Xu, Y.; Chen, Z.; Wang, T.; Zhang, H. *J. Phys. Chem. C* **2007**, *111*, 5034–5038.
(6) Jia, C. J.; Sun, L. D.; Yan, Z. G.; You, L. P.; Luo, F.; Han, X. D.; Pang, Y. C.; Zhang, Z.; Yan, C. H. *Angew. Chem., Int. Ed.* **2005**, *44*, 4328.
(7) Lv, B.; Xu, Y.; Wu, D.; Sun, Y. *Particuology* **2008**, *6*, 334.
(8) Lu, L.; Ai, Z.; Li, J.; Zheng, Z.; Li, Q.; Zhang, L. *Cryst. Growth Des.* **2007**, *7*, 459.
(9) Wang, H.; Brandl, D. W.; Le, F.; Nordlander, P.; Halas, N. J. *Nano Lett.* **2006**, *6*, 827.
(10) Li, S.; Zhang, H.; Wu, J.; Ma, X.; Yang, D. *Cryst. Grow. Des.* **2006**, *6*, 351.
(11) Cozzoli, P. D.; Snoeck, E.; Garcia, M. A.; Giannini, C.; Guagliardi, A.; Cervellino, A.; Gozzo, F.; Hernando, A.; Achterhold, K.; Ciobanu, N.; Parak, F. G.; Cingolani, R.; Manna, L. *Nano Lett.* **2006**, *6*, 1966.
(12) Lee, S. H.; Liddell, C. M. *Small* **2009**, *5*, 1957.
(13) Zeng, S.; Tang, K.; Li, T.; Liang, Z.; Wang, D.; Wang, Y.; Qi, Y.; Zhou, W. J. *Phys. Chem. C* **2008**, *112*, 4836–4843.
(14) Li, X.; Yu, Xin.; He, J.; Xu, Z. *J. Phys. Chem. C* **2009**, *113*, 2837–2845.
(15) Maruthamuthu, P.; Gurunathan, K.; Subramanian, E.; Ashokkumar, M. *Bull. Chem. Soc. Jpn.* **1991**, *64*, 1933.
(16) Wang, G.; Gou, X.; Horvat, J.; Park, J. *J. Phys. Chem. C* **2008**, *112*, 15220.
(17) Rhodes, F. H.; Burr, C. R.; Webster, P. A. *Ind. Eng. Chem.* **1924**, *16*, 960.
(18) Yigit, M. V.; Mazumdar, D.; Lu, Y. *Bioconjugate Chem.* **2008**, *19*, 412.
(19) Mahmoudi, M.; Simchi, A.; Imani, M.; Hfeli, U. O. *J. Phys. Chem. C* **2009**, *113*, 8124.
(20) Khedra, M. H.; Halimb, K.S. A.; Soliman, N. K. *Mater. Lett.* **2009**, *63*, 598.
(21) Mohapatra, S. K.; John, S. E.; Banerjee, S.; Misra, M. *Chem. Mater.* **2009**, *21*, 3048.
(22) Tahir, A. A.; Wijayantha, K. G. U.; Yarahmadi, S. S.; Mazhar, M.; McKee, V. *Chem. Mater.* **2009**, *21*, 3763.
(23) Cesar, I.; Kay, A.; Martinez, J. A. G.; Gratzel, M. *J. Am. Chem. Soc.* **2006**, *128*, 4582.
(24) Luo, W.; Wang, D.; Wang, F.; Liu, T.; Cai, J.; Zhang, L.; Liu, Y. *Appl. Phys. Lett.* **2009**, *94*, 202507.
(25) Hu, Y. S.; Shwarsctein, A. K.; Forman, A. J.; Hazen, D.; Park, J. N.; McFarland, E. W. *Chem. Mater.* **2008**, *20*, 3803.
(26) Aroutiouniana, V. M.; Arakelyana, V. M.; Shahnazaryana, G. E.; Stepanyana, G. M.; Turnerb, J. A.; Khaselev, O. *Int. J. Hydrogen Energy* **2002**, *27*, 33.
(27) Vayssies, L.; Sathe, C.; Butorin, S. M.; Shuh, D. K.; Nordgren, J.; Guo, J. *Adv. Mater.* **2005**, *17*, 2320.
(28) Liu, Z.; Subramaniam, V.; Misra, M. *J. Phys. Chem. C.* **2009**, *113*, 14028.
(29) Cornell R. M., Schwertmann U. *The Iron Oxide Book*, 2nd ed.; Wiley-VCH: Weinheim, Germany, 2003; p 147.
(30) Angwafor, N. G. N.; Riley, D. J. *Phys. Stat. Sol.* **2008**, *205*, 2351–2354.
(31) Cho, I. S.; Lee, S.; Noh, J. H.; Kim, D. W.; Jung, H. S.; Kim, D. W.; Hong, K. S. *Cryst. Growth Des.* **2010**, *10*, 2427–2450.
(32) Bhargava, G.; Gouzman, I.; Chun, C. M.; Ramanarayanan, T. A.; Bernasek, S. L. *Appl. Surf. Sci.* **2007**, *253*, 4322–4329.
(33) Yamashita, T.; Hayes, P. *Appl. Surf. Sci.* **2008**, *254*, 2441–2449.
(34) Grosvenor, A. P.; Kobe, B. A.; Biesinger, M. C.; Mclntyre, N. S. *Surf. Interface Anal.* **2004**, *36*, 1564–1574.
(35) Hon, Y. H.; Taylor, A.; Mantle, M. D.; Knowles, K. M. *J. Non-cryst. Solids* **2007**, *353*, 313–320.
(36) Quinan, J. R.; Wiberley, S. E. *Anal. Chem.* **1954**, *26*, 1762–1764.
(37) Zhao, B.; Wang, Y.; Guo, H.; Wang, J.; He, Y.; Jiao, Z.; Wu, M. *Mater. Sci. Poland* **2007**, *25*, 1143–1148.
(38) Li, L.; Keying, S. *Chem. Res. Chin. Univ.* **2009**, *25*, 595–599.
(39) Zhang, Z. J.; Mei, X. J.; Fen, L. R.; Lu, S. J.; Qiu, F. L. *Chin. Chem. Lett.* **2004**, *15*, 867–870.
(40) Naik, B.; Parida, K. M. *Ind. Eng. Chem. Res.* **2010**, *49*, 8339–8346.
(41) Hochbaum, A. I.; Yang, P. *Chem. Rev.* **2010**, *110*, 527–546.